PNAS RESEARCH ARTICLE | EARTH, ATMOSPHERIC, AND PLANETARY SCIENCES

Summer and nonsummer climatic signals in speleothem $\delta^{18}O$ revealed by loess microcodium $\delta^{18}O$ in East Asia

Zeke Zhang[a,b,1], Zhengyu Liu[c,d], Gaojun Li[b], Yanjun Cai[e,1], Qin Wen[d], Hai Cheng[e], R. Lawrence Edwards[f], Jing Lei[a,g], Heng Liu[a,g], Zhaowei Jing[h], Tao Li[i], Steven C. Clemens[j], Yongjin Wang[d], Youbin Sun[a], Zhengguo Shi[a,e], Liangcheng Tan[a,e], Shugang Kang[a], Xulong Wang[a], Zhangdong Jin[a,e], Weijian Zhou[a,e,k], and Zhisheng An[a,e,l,1]

Affiliations are included on p. 7.

Contributed by Zhisheng An; received December 10, 2024; accepted June 12, 2025; reviewed by Dabang Jiang and Michael Rogerson

Speleothem $\delta^{18}O$ records from central southern China have long been regarded as a key benchmark for Asian summer monsoon intensity. However, the similar $\delta^{18}O$ minima observed among precession minima and their link to seasonal precipitation mixing remains unclear. Here, we present a 400,000-y record of summer precipitation $\delta^{18}O$ from loess microcodium, which captures distinct precession cycles similar to those seen in speleothem $\delta^{18}O$ records, particularly during glacial periods. Notably, our microcodium $\delta^{18}O$ record reveals very low-$\delta^{18}O$ values during precession minima at peak interglacials, a feature absent in speleothem $\delta^{18}O$ records from central southern China. This discrepancy suggests that the mixed summer and nonsummer climatic signals substantially influence the speleothem $\delta^{18}O$ records from central southern China. Proxy-model comparisons indicate that the lack of very low-$\delta^{18}O$ values in speleothem $\delta^{18}O$ records is due to an attenuated summer signal contribution, resulting from a lower summer-to-annual precipitation ratio in southern China at strong monsoon intervals. Our findings offer a potential explanation for the long-standing puzzle of the absence of 100- and 41-kyr cycles in speleothem $\delta^{18}O$ records and underscore the critical role of seasonality in interpreting paleoclimatic proxies in central southern China. These insights also have broader implications for interpreting speleothem $\delta^{18}O$ records globally, advocating for a more multiseason interpretive framework.

monsoon | oxygen isotope | speleothem | seasonality | orbital timescale

Significance

For decades, scientists have struggled to explain why Chinese cave oxygen isotope records fail to show the clear impact of ice age cycles associated with Earth's orbit changes, which otherwise offer valuable insights into the Asian summer monsoon and natural climate changes. By studying calcium carbonate in windblown dust deposits northwest of the cave sites, we identified distinct signatures of these ice age cycles that were absent in the cave oxygen isotope records. Combined with climate simulations, we demonstrate that the cave oxygen isotope records from southeast China incorporate precipitation signals from different seasons rather than reflecting exclusively summer precipitation. This breakthrough has broader implications for interpreting cave oxygen isotope records worldwide by emphasizing the role of precipitation seasonality.

Intensive investigations of geological records have greatly advanced our understanding of the East Asian Summer Monsoon (EASM) dynamics at orbital timescale. Speleothem oxygen isotope ratios ($\delta^{18}O$) records from East Asia, in particular, have become a benchmark for the EASM intensity, and have been interpreted as reflecting responses predominantly to summer insolation changes at orbital timescale (1–7). One outstanding problem, however, has been that the similar $\delta^{18}O$ values among different precession minima in the speleothem $\delta^{18}O$ records from central southern China differ substantially from the variation of summer insolation maxima (Fig. 1*D* orange vs. Fig. 1*E*). Furthermore, other monsoon-related proxy records (8–14), including speleothem $\delta^{18}O$ records from the low-latitude monsoon region (15, 16) (Fig. 1*F*), clearly show fluctuating values among precession minima. These fluctuations are likely forced by changes in insolation as well as atmospheric CO_2 concentration (17) and continental ice sheets (18). Therefore, it remains puzzling why the speleothem $\delta^{18}O$ records from central southern China show similar $\delta^{18}O$ minima among precession minima, in particular, the $\delta^{18}O$ value during precession minima at peak interglacial is similar to those during other precession minima intervals (15, 16, 19).

This puzzle raises questions regarding the paleoclimatic interpretation of speleothem $\delta^{18}O$ records from central southern China (10, 11, 22–24). Most previous studies on speleothem $\delta^{18}O$ have focused on hydrological processes related to precipitation $\delta^{18}O$, such as changes of moisture sources (25, 26) and upstream depletion in source regions (27, 28) or between sources and caves (2, 15, 16). In particular, changes in speleothem $\delta^{18}O$ have continued to be interpreted as dominated by summer-season precipitation $\delta^{18}O$ [e.g., (1–4)] even though there are indications of contributions from nonsummer precipitation, such as winter precipitation (29), in cave drip-water $\delta^{18}O$ in modern observations (30, 31), annually banded speleothem $\delta^{18}O$ analysis (32) and model simulations (33–36). Partly, this uncertainty reflects the difficulty of deciphering the seasonal contributions of summer and nonsummer precipitation to speleothem $\delta^{18}O$ records, because of the lack of long-term geological records that can clearly reflect the changes in summer precipitation $\delta^{18}O$.

Reviewers: D.J., Institute of Atmospheric Physics, Chinese Academy of Sciences; and M.R., Northumbria University.

The authors declare no competing interest.

[1]To whom correspondence may be addressed. Email: zhangzk@ieecas.cn, yanjun_cai@xjtu.edu.cn, or anzs@loess.llqg.ac.cn.

This article contains supporting information online at https://www.pnas.org/lookup/suppl/doi:10.1073/pnas.2425565122/-/DCSupplemental.

Published July 11, 2025.

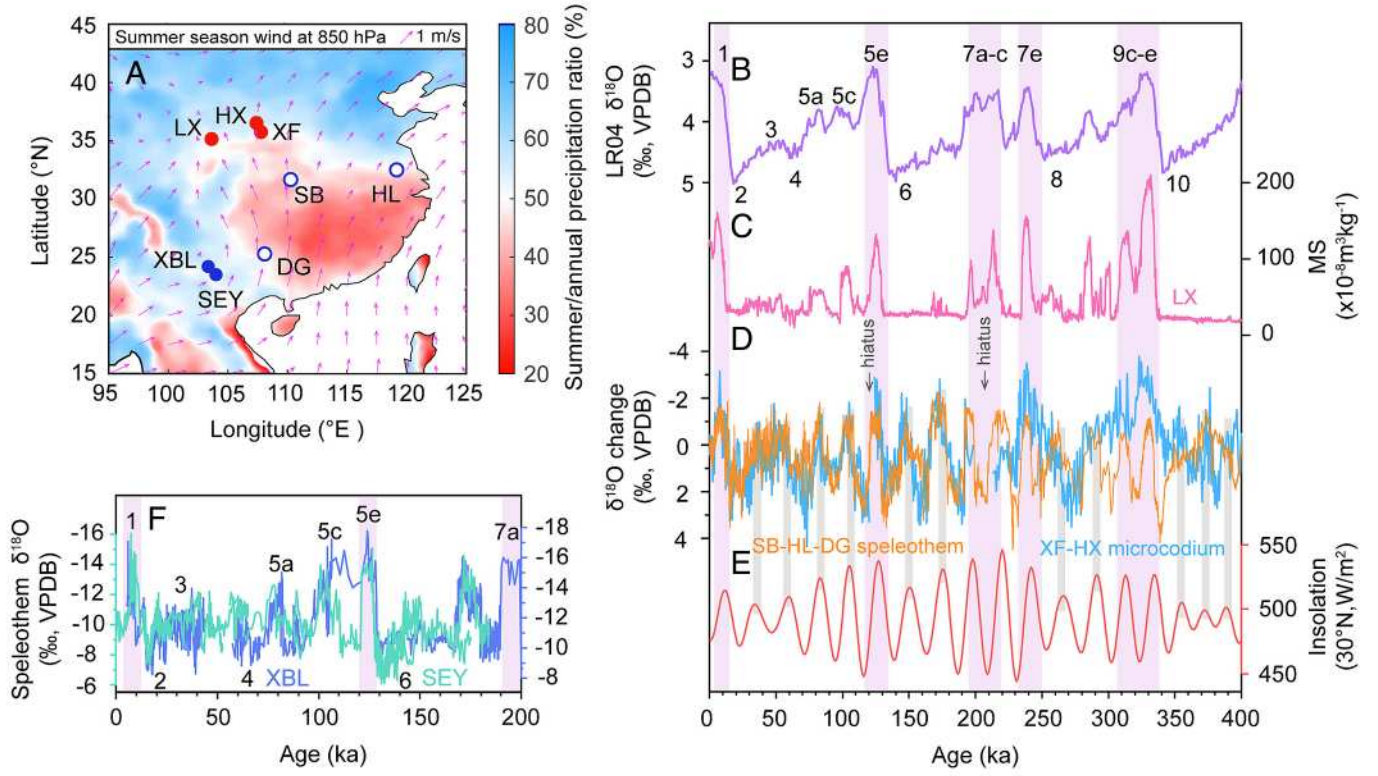

Fig. 1. Locations and $\delta^{18}O$ records in the EASM region. (*A*) Locations of $\delta^{18}O$ records with similar or distinctly fluctuating $\delta^{18}O$ minima among precession minima (open or solid circles) on a map showing average modern climatology. Particularly, speleothem $\delta^{18}O$ records from central southern China show similar $\delta^{18}O$ minima among precession minima (1) (blue open circles), where summer precipitation accounts for less than half of the annual precipitation. Blue and red circles represent locations of caves and loess sections, respectively. (*B–E*) Comparison of microcodium $\delta^{18}O$ record with other records. (*B*) Composite of benthic $\delta^{18}O$ (LR04, purple) (18). Labeled is the marine isotope stage (MIS) of benthic $\delta^{18}O$. (*C*) Magnetic susceptibility (MS) variations at the Linxia (LX) section on the western CLP (pink) (20). (*D*) Relative change with respect to the beginning of each record (mean of 0 to 1 kyr) of microcodium $\delta^{18}O$ records (blue) in this study from Xifeng (XF) and Huanxian (HX) sections on the central CLP and speleothem $\delta^{18}O$ records from central southern China [orange, composed based on Sanbao (SB), Hulu (HL), and Dongge (DG) speleothem $\delta^{18}O$ records in Cheng et al., (2016) (1). (*E*) Summer (June 21st) insolation at 30 °N (red) (21). (*F*) Speleothem $\delta^{18}O$ records from southwestern China [blue, Xiaobailong (XBL) (15) and cyan, Southeastern Yunnan (SEY) (16). Pink bands represent precession minima at peak interglacial periods when a major difference between microcodium and speleothem $\delta^{18}O$ records occurs. Gray bands represent high summer insolation periods. Climate data are from NCEP/NCAR Reanalysis 1 and GPCC data provided by the NOAA PSL, Boulder, CO, from their website at https://psl.noaa.gov. Average spring (March, April, and May) and summer (June, July, and August) precipitation and summer wind fields at 850 hPa are based on 1891 to 2018 and 1948 to 2014 periods, respectively.

Recently a new type of $\delta^{18}O$ proxy, based on the oxygen isotope composition of microcodium from Chinese loess-paleosol sequences, has been used to reconstruct long-term changes in summer precipitation $\delta^{18}O$ (37–39) (*SI Appendix, Supplemental note* 1). Microcodium is a calcite microformation which is found in the Chinese loess and shows a cell-like structure under a binocular microscope (*SI Appendix*, Fig. S1*B*), and thus has been suggested as biological cells replaced with authigenic calcite (40). The in-situ microcodium in the topsoil has been shown to resemble plant root structure (*SI Appendix*, Fig. S1*C*). This suggests that microcodium is formed by the calcification of plant root cells on the Chinese Loess Plateau (CLP). The very low $\delta^{18}O$ value of microcodium from modern soil matches well with the calculated $\delta^{18}O$ values of calcite precipitating during summer season and the calcite crystallized at other seasons on the CLP is characterized by much higher calculated $\delta^{18}O$ values, suggesting that microcodium precipitates during the summer season (37). This is also consistent with the suggestion of summer formation of calcite according to the clumped isotope thermometry, and the climate change in summer on the CLP from wet to dry conditions and thus depleted soil moisture (39) (*SI Appendix, Supplemental note* 1). In addition, the large amplitude difference (~7‰) in microcodium $\delta^{18}O$ records since the last interglacial suggests that microcodium $\delta^{18}O$ predominantly reflects precipitation $\delta^{18}O$ signal (37–39), since the presumed maximal 8°C difference would only lead to a variation of about 1.8‰. The microcodium $\delta^{18}O$ record since the last interglacial (38) shows distinct precession cycles as seen in speleothem $\delta^{18}O$ records. More interestingly, it exhibits distinct fluctuations in $\delta^{18}O$ minima among precession minima. Therefore, a comparative study of microcodium and speleothem $\delta^{18}O$ records spanning multiple glacial-interglacial cycles may have the potential to reconcile the disparities observed in these two archives by discriminating the seasonal contributions of summer and nonsummer precipitation.

To explore these disparities, we collected loess samples from the well-studied Xifeng (XF) section (35°45'N, 107°47'E) located in the central CLP (Fig. 1*A*). The loess chronology was established by correlating the loess-paleosol sequences of the XF section with previously published sections in the Dongzhiyuan high tableland and benthic $\delta^{18}O$ records along with the OSL dates of local loess-paleosol profile (*Materials and Methods*). Microcodium was picked at 5-cm resolution for measurements of oxygen isotopes ($\delta^{18}O$). A total of 437 samples were analyzed (*Materials and Methods*), giving a mean resolution of ~500 y. We extended the XF microcodium $\delta^{18}O$ record to the past 400 kyr and integrated these new data with previously published data (37, 38), providing a new composite microcodium $\delta^{18}O$ record of the past 400 kyr (Fig. 1*D* and *Materials and Methods*).

Results

Our microcodium $\delta^{18}O$ changes closely align with variations in summer insolation: lower $\delta^{18}O$ values occur during periods of high summer insolation (Fig. 1 *D* and *E*), consistent with speleothem

$\delta^{18}O$ records from central southern China (Fig. 1*D*). Especially during the last and penultimate glacial periods, the magnitude of variability in microcodium $\delta^{18}O$ is generally comparable to that observed in speleothem $\delta^{18}O$. These similarities suggest that both the microcodium and speleothem $\delta^{18}O$ records capture a shared signal in precipitation $\delta^{18}O$ changes.

A more careful comparison of the two $\delta^{18}O$ records, however, shows one distinct difference. The $\delta^{18}O$ minima among precession minima remain similar in the speleothem $\delta^{18}O$ record from central southern China (Fig. 1*D*, orange), but exhibit very low-$\delta^{18}O$ values in the microcodium $\delta^{18}O$ record at the peak interglacials associated with MIS 1, 5e, 7e, and 9c-d, and minor hiatuses during MIS 5e and 7a-c (Fig. 1*D*, blue).

Discussion

Lower $\delta^{18}O$ Values During Precession Minima at Peak Interglacials. The $\delta^{18}O$ minima difference during precession minima at peak interglacials between the two $\delta^{18}O$ records may partly originate from the two different proxy systems. Under equilibrium conditions, the $\delta^{18}O$ of calcite is related to the $\delta^{18}O$ of water and temperature-dependent fractionation between water and calcite (41). Microcodium is suggested to precipitate during the summer season (37), and thus its equilibrium fractionation is likely to be determined by summer temperature. The cave temperature is approximately the regional mean annual temperature (42), and thus the speleothem's equilibrium fractionation is determined by mean annual temperature. The systematic difference between summer temperature on the CLP and mean annual temperature in central southern China would only lead to a systematic deviation in absolute values and does not change the variability. Assuming that the annual temperature in central southern China is more stable and the change in summer temperature on the CLP is large at glacial-interglacial timescale, high summer temperature during peak interglacials would lead to a small fractionation factor (41) and thus a negative microcodium $\delta^{18}O$ value. However, the microcodium $\delta^{18}O$ value of the MIS 5e is more negative than that of the MIS 5a and 5c by about 2‰. At least a temperature difference of 8°C between the MIS 5e and 5a/5c is required to explain such a large $\delta^{18}O$ discrepancy, while the temperature record based on soil bacterial lipid signatures shows a similar temperature between the MIS 5e and 5a/5c on the CLP (43). Therefore, the $\delta^{18}O$ minima difference between the two $\delta^{18}O$ records is not mainly due to the different proxy systems and largely reflects the difference in precipitation $\delta^{18}O$.

Lower $\delta^{18}O$ values during precession minima at peak interglacials in microcodium $\delta^{18}O$ indicate a stronger summer monsoon intensity, as supported by the speleothem records from southwestern China (Fig. 1*F*) and most other EASM precipitation records from northern China (*SI Appendix*, Fig. S2), particularly a summer monsoon record based on loess magnetic susceptibility from the western CLP (20) (Fig. 1*C*). The western CLP is located at the northwestern margin of the EASM, and therefore it is likely that only the strongest summer monsoon could reach this region (44), driving pedogenesis. Thus, the magnetic susceptibility record there well records the strongest EASM that are associated with high magnetic susceptibility values during precession minima at peak interglacials, consistent with the lower $\delta^{18}O$ values in microcodium $\delta^{18}O$ record. Moreover, during MIS 5e and 7a-c, the hiatuses also indicate the strongest EASM intensity and pedogenesis (*SI Appendix*, Fig. S3 *B* and *C*), which led to the dissolution of microcodium. In addition, the hiatus of Xiaotian (XT) speleothem $\delta^{18}O$ record (45) and the anomalously high ^{232}Th concentrations associated with a dark-colored "dirty" portion of Zhenzhu (ZZ) speleothem (46) during MIS 5e from northern China also suggest stronger rainfall. This could lead to either an undersaturation of Ca^{2+} in dripwater or flooding in XT cave (45) and a high input of detrital material in the ZZ cave, respectively (*SI Appendix*, *Supplemental note* 2 and Figs. S4 and S5).

The agreement between lower precipitation $\delta^{18}O$ values in microcodium $\delta^{18}O$ record and the more substantial monsoon precipitation inferred from other proxy records in northern China is well supported by model simulations in which the $\delta^{18}O$ signal represents the intensity of the EASM system (27, 47). The strong summer monsoon can be characterized by enhanced southerly monsoon winds, transporting moisture further into northern China and thus correlating strongly with negative summer monsoon precipitation $\delta^{18}O$ over China and enhanced monsoon rainfall in northern China (27). In turn, this agreement confirms that microcodium $\delta^{18}O$ record reflects more clearly changes in summer season precipitation $\delta^{18}O$ in the EASM region than speleothem $\delta^{18}O$ record from central southern China. The $\delta^{18}O$ minima difference during precession minima at peak interglacials between microcodium and speleothem $\delta^{18}O$ records implies the potential influence of mixed summer and nonsummer climatic signals on speleothem $\delta^{18}O$.

Summer and Nonsummer Signal Contributions to Speleothem $\delta^{18}O$. The $\delta^{18}O$ minima difference during precession minima at peak interglacials between the two $\delta^{18}O$ records is unlikely to be caused by the changes in moisture sources or the summer-only precipitation $\delta^{18}O$ changes due to spatial difference of summer precipitation in the EASM region. The caves in southwestern China and central southern China, and the CLP are successively located along the summer monsoon moisture trajectory (Fig. 1*A*). First, although the change in moisture sources may be an important factor of the precipitation $\delta^{18}O$ (45), it would generate similar features in precipitation $\delta^{18}O$ in East Asia and thus both speleothem and microcodium $\delta^{18}O$ records. Therefore, it cannot explain this difference solely and an additional mechanism is needed. Second, this difference cannot be caused by monsoon hydrological processes from moisture sources to the caves in central southern China, which would also generate similar features in both speleothem and microcodium $\delta^{18}O$ records. Third, this difference cannot result from monsoon hydrological processes en-route from the caves in central southern China to the CLP. In that case, summer monsoon precipitation in central southern China should exhibit similar values among precession minima. However, the upstream speleothem $\delta^{18}O$ records from southwestern China display fluctuating $\delta^{18}O$ minima among precession minima (15, 16) (Fig. 1*F*), which should be inherited by the speleothem $\delta^{18}O$ records in central southern China. Data-model comparisons also suggest that precipitation $\delta^{18}O$ should be coherent along the monsoon moisture trajectory and representative of the overall EASM intensity, as defined by the large-scale monsoon circulation (27, 47–49), even in the presence of regional precipitation differences.

We propose that the $\delta^{18}O$ minima difference during precession minima at peak interglacials between the two $\delta^{18}O$ records is caused by the changes in seasonal signal contributions of summer and nonsummer precipitation to the speleothem $\delta^{18}O$, including precipitation amount and precipitation $\delta^{18}O$. Modern monitoring observations show that precipitation $\delta^{18}O$ outside the cave displays distinct seasonal changes in the EASM region. However, the $\delta^{18}O$ of about 82% of the drip sites inside the cave is almost constant year-round, indicating that drip water is a mixture of precipitation integrated over relatively long periods (30), except for a few drip sites that exhibit a slight bias due to some hydrological processes in the cave system (e.g., flow switching in the

karst or evaporation inside the cave) (50). Moreover, Baker et al. (31) analyzed 163 drip sites from 39 global caves and showed a 1:1 linear relationship between drip-water $\delta^{18}O$ and amount-weighted annual precipitation $\delta^{18}O$, supporting cave drip-water $\delta^{18}O$ primarily as a consequence of the accumulation of multiseasonal precipitation signals. In southeastern China, in the regions where the speleothem $\delta^{18}O$ records are derived (such as Hulu, Sanbao, and Dongge), analyses of modern rainfall indicate that while summer monsoon precipitation accounts for approximately 32 to 52% of the annual total, spring, autumn, and winter precipitation contribute 22 to 38%, 12 to 24%, and 6 to 17%, respectively (*SI Appendix*, Fig. S6). The nonsummer precipitation amount is close to or even higher than the summer precipitation (Fig. 1*A* and *SI Appendix*, Fig. S6). Furthermore, the precipitation $\delta^{18}O$ values in nonsummer seasons, in particular in spring (~−3‰), are much more positive than in summer (~−9‰) (*SI Appendix*, Fig. S6). As a result, the amount-weighted annual precipitation $\delta^{18}O$ value is more positive than the summer precipitation $\delta^{18}O$ value there (*SI Appendix*, Fig. S7). Therefore, the change in seasonal signal contributions of summer and nonsummer precipitation to the speleothem $\delta^{18}O$ is a potentially important factor for the $\delta^{18}O$ minima difference during precession minima at the peak interglacials between the microcodium and speleothem $\delta^{18}O$ records.

The influence of the changes in seasonal signal contributions of summer and nonsummer precipitation to the speleothem $\delta^{18}O$ in central southern China is confirmed by an all-forcing 150 kyr simulation forced by the Earth's orbital parameters, greenhouse gases, and global ice sheets in the isotope-enabled Community Earth System Model (iCESM1.3, *Materials and Methods*). In the all-forcing experiment, the correlation coefficient between summer and amount-weighted annual precipitation $\delta^{18}O$ changes over the past 150 kyr shows different spatial characteristics, although the correlations are all significant ($P < 0.01$) in the EASM regions (Fig. 2). Over northern and southwestern China, the correlation coefficients exceed 0.7 (Fig. 2*A*), consistent with the modern observation that the calculated amount-weighted annual mean precipitation $\delta^{18}O$ value is close to summer precipitation $\delta^{18}O$ value there (*SI Appendix*, Fig. S7), due to the concentrated precipitation during summer season and limited nonsummer (in particular spring) precipitation (Fig. 1*A* and *SI Appendix*, Fig. S8). In contrast, over most of southeastern to central China, where the speleothem $\delta^{18}O$ record is derived, the correlation coefficient ranges from ~0.5 to ~0.7, which is lower than in northern and southwestern China (Fig. 2*A*). This lower correlation coefficient can be attributed to the low ratio of summer signal contribution to the amount-weighted annual precipitation $\delta^{18}O$ (Fig. 2 *B* and *C*). The summer signal contribution is calculated by multiplying the summer precipitation $\delta^{18}O$ by the summer-to-annual precipitation ratio and the amount-weighted annual precipitation $\delta^{18}O$ is the sum of four seasonal signal contributions. It is worth noting that the ratio of summer signal contribution to the annual precipitation $\delta^{18}O$ during the MIS 5e (Fig. 2*B*) is close to that during the Last Glacial Maximum (LGM) (Fig. 2*C*), indicating that the summer signal contribution to the annual precipitation $\delta^{18}O$ did not increase with the strengthening of summer monsoon intensity from the LGM to MIS 5e.

To better understand the differences between summer and annual $\delta^{18}O$ in the southeastern to central southern China region, we further analyzed the modeled seasonal precipitation amount and seasonal precipitation signal contributions to the annual $\delta^{18}O$ there over the past 150 kyr (Fig. 3). The discrepancy between summer and annual $\delta^{18}O$ changes typically occurs during strong monsoon intervals, characterized by very low values of summer precipitation $\delta^{18}O$ during precession minima (Fig. 3*A*, pink bands). This pattern is analogous to the $\delta^{18}O$ minima difference observed during precession minima at the peak interglacials between our microcodium and speleothem $\delta^{18}O$ records discussed above. It is worth noting that the summer precipitation signal contribution to the annual precipitation $\delta^{18}O$ shows similar values among precession minima (Fig. 3*D*, blue). During the strong monsoon intervals, although the summer precipitation $\delta^{18}O$ minima are relatively lower (Fig. 3*A*, blue), the summer signal contribution to the annual precipitation $\delta^{18}O$ does not increase with increased monsoon intensity (Fig. 3*D*, blue). In addition, the nonsummer precipitation also has an important contribution to the annual precipitation $\delta^{18}O$ and may partly contribute to the discrepancy between summer and annual $\delta^{18}O$ changes, although the autumn precipitation signal contribution seems to partly offset the change in the spring precipitation signal contribution (Fig. 3*D*).

The attenuated summer precipitation signal contribution to the annual precipitation $\delta^{18}O$ can be attributed to the lower summer-to-annual precipitation ratio in southern China at the strong monsoon intervals. It is worth noting that summer precipitation in southern China is out of phase with the overall EASM intensity inferred from summer precipitation $\delta^{18}O$ (Fig. 3 *A* and *B*). This dipole rainfall response has been found in modern meteorological observations and is robust across climate models (27, 47, 51); it has also been inferred from cave moisture proxy records in the central southern China

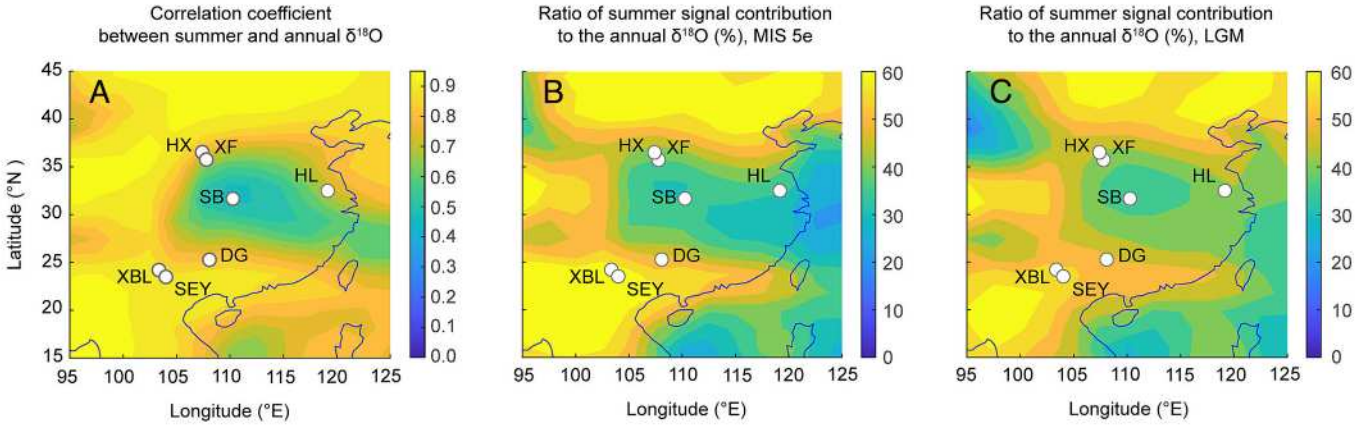

Fig. 2. Simulated summer and annual precipitation $\delta^{18}O$ changes during the past 150 kyr in the EASM region in the all-forcing experiment. (*A*) A map shows the correlation coefficient between simulated summer and annual precipitation $\delta^{18}O$ changes over the past 150 kyr. The region where the speleothem $\delta^{18}O$ records are derived shows a weaker correlation coefficient compared to northern and southwestern China. Gray open circles show the locations mentioned in this study. (*B* and *C*) The ratio of summer signal contribution to the annual precipitation $\delta^{18}O$ during the MIS 5e (*B*) and LGM (*C*). The summer signal contribution is calculated by multiplying the summer precipitation $\delta^{18}O$ by the summer-to-annual precipitation ratio.

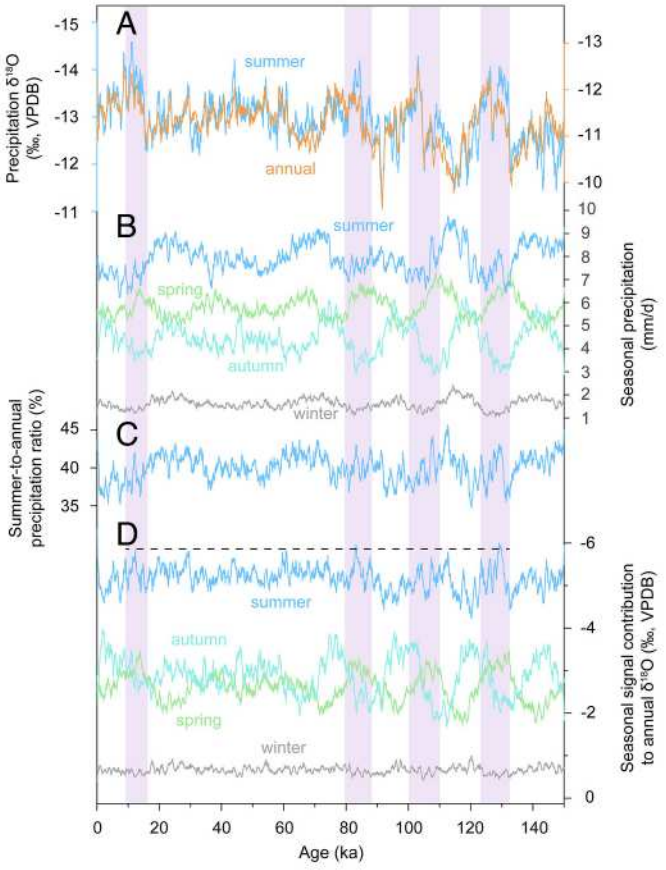

Fig. 3. Modeled contributions of summer and nonsummer precipitation to the annual $\delta^{18}O$ in the central southern China region in the all-forcing experiment. (*A*) Simulated summer (JJA, blue) and annual precipitation $\delta^{18}O$ (amount-weighted, orange) over the past 150 kyr. (*B*) Simulated spring (MAM), summer (JJA), autumn (SON), and winter (DJF) precipitation over the past 150 kyr. (*C*) Simulated summer-to-annual precipitation ratio. (*D*) Simulated spring (MAM), summer (JJA), autumn (SON), and winter (DJF) precipitation signal contributions to the annual $\delta^{18}O$ over the past 150 kyr, which are the seasonal precipitation $\delta^{18}O$ multiplied by the corresponding seasonal to annual precipitation ratio. Pink bands indicate the strong monsoon intervals with a discrepancy in $\delta^{18}O$ minima between summer and annual precipitation $\delta^{18}O$ changes during precession minima. The dash black line shows the similar contributions of summer signal to annual $\delta^{18}O$ among precession minima.

region (52). Dynamically, a stronger EASM system enhances the northward moisture transport, resulting in moisture convergence and, in turn, precipitation in northern China and the opposite in central southern China. This decreased summer precipitation leads to a lower summer-to-annual precipitation ratio in southern China (Fig. 3*C*). As such, the lower summer-to-annual precipitation ratio substantially offsets the effect of low summer precipitation $\delta^{18}O$, resulting in an attenuated summer precipitation signal contribution to the annual precipitation $\delta^{18}O$ at strong monsoon intervals and thus the similar contributions of summer precipitation signal among precession minima (Fig. 3*D*, blue).

Implication to Monsoon Dynamics and Interpretation of Speleothem $\delta^{18}O$ Records. The stronger summer monsoon intensity during precession minima at peak interglacials recorded by microcodium $\delta^{18}O$ record agrees well with other monsoon precipitation records from northern China (*SI Appendix*, Fig. S2), suggesting that the EASM is controlled by both summer insolation and changes in ice volume/atmospheric CO_2 concentration at glacial-interglacial timescale. Dynamically, monsoon circulation is driven primarily by the land-sea thermal contrast, and affected by the position of westerlies (36) and latitudinal insolation gradient (53), which can be influenced by orbital insolation (41 and 23 kyr) and glacial boundary conditions/atmospheric CO_2 concentration (100 and 41 kyr) (44, 54–56). The coexistence of the 100-, 41-, and 23-kyr periods in microcodium $\delta^{18}O$ is more in line with most other proxy monsoon records and monsoon dynamics than the only 23-kyr period in speleothem $\delta^{18}O$ (*Materials and Methods* and *SI Appendix*, Fig. S9). The roles of glacial boundary conditions and atmospheric CO_2 concentration on the summer precipitation $\delta^{18}O$ have been confirmed by the attenuated precession minima during the last glacial period in all-forcing model simulation, compared to that in the orbital-only forcing simulation (*Materials and Methods* and *SI Appendix*, Fig. S10). The lack of attenuated precession $\delta^{18}O$ minima during the MIS 5a and 5c, as opposed to the MIS 5e, in all-forcing model simulation is probably due to the uncertainty of ice sheet reconstructions in the model simulation (*Materials and Methods*).

Our finding offers a potential mechanistic explanation for the lack of 100- and 41-kyr cycles in the speleothem $\delta^{18}O$ records from central southern China. Small ice volume/high atmospheric CO_2 concentration during peak interglacial and high obliquity would lead to a large land-sea thermal contrast, thus a strong EASM intensity (53–56) and low summer precipitation $\delta^{18}O$ values. Meanwhile, the strong EASM system enhances the northward moisture transport and decreases the summer precipitation and, thus, the summer-to-annual precipitation ratio in central southern China. The lower summer-to-annual precipitation ratio in the cave dripwater could offset the effect of low summer precipitation $\delta^{18}O$ values, and thus attenuate the summer precipitation signal contribution and the 100- and 41-kyr cycles in the speleothem $\delta^{18}O$ records in central southern China. In the future, isotope-enabled climate model simulations spanning multiple glacial-interglacial cycles are critically indispensable to quantitatively assess the influences of summer and nonsummer signal contributions on the periods of speleothem $\delta^{18}O$ records. In addition, our insight also has broader implications for interpreting speleothem $\delta^{18}O$ records worldwide, emphasizing the importance of considering the seasonality when interpreting paleoclimatic proxies.

Materials and Methods

Setting, Sampling, and Chronology. Loess samples for microcodium isotope analysis in this study were collected from the Xifeng (XF) section (35°45′N, 107°47′E) located in the central CLP (Fig. 1*A*). This regional climate is a typical monsoon climate characterized by hot and rainy summers and cold and dry winters (*SI Appendix*, Fig. S8). Modern, mean annual temperature is approximately 9.2 °C, and mean annual precipitation is approximately 528 mm. The XF section in this study is located between the Zhaojiachuan (ZJC, 35°45′N, 107°49′E) (57), Caijiazui (CJZ, 35°48′N, 107°36′E) (14) and Chengjiazhuang (CHJZ, 35°45′N, 107°41′E,) (58) sections, near Qingyang City within the Dongzhiyuan high tableland, which is the largest loess high tableland (~900 km^2) composed of alternating loess and paleosol layers with a thickness of about 200 m and flat top surfaces in the center CLP. Currently, erosion has caused the plateau to be relatively fragmented. The loess-paleosol stratigraphy of these sections can be well correlated through iconic paleosol layers (S_2 and S_5) and magnetic susceptibility records (*SI Appendix*, Fig. S11). Magnetic susceptibility is the most accurate, objective, and easily reproducible delimitation of the loess and paleosol units (58). The paleosol layers exhibit high magnetic susceptibility values due to stronger pedogenesis associated with stronger summer monsoon and lower dust accumulation during interglacial periods, and the loess layers show lower magnetic susceptibility values (59). It is obvious that the four loess-paleosol couplets in our XF section align with the top four loess-paleosol layers from the Brunhes chron in the other three sections.

Correlations between Chinese loess and the climatic record from deep-sea sediments over the last 2.6 My have suggested that the Chinese loess-paleosol

sequence documented multiple glacial and interglacial cycles (60). Paleosol (loess) layers with high (low) magnetic susceptibility values correspond to interglacial (glacial) periods, which have been validated by several independent loess chronology methods. In the Dongzhiyuan high tableland, the age model for the CHJZ section was established based on the susceptibility time scale within the framework of paleomagnetic reversals, showing remarkable parallels between magnetic susceptibility and benthic $\delta^{18}O$ records (58). Subsequently, an improved astronomical timescale for the ZJC section was achieved by tuning the grain size records to orbital obliquity and precession and is supported by magnetic reversal boundaries (57) (*SI Appendix*, Fig. S11*B*). Recently, by correlating loess grain size with the benthic $\delta^{18}O$ records and further tuning the age model to the absolute-dated speleothem $\delta^{18}O$ records at the precession band, 13 successive geomagnetic excursions in the Brunhes chron were identified comparing the $^{10}Be_{GM}$ flux (geomagnetic field-induced ^{10}Be production rate) peaks in the CJZ section with global geomagnetic records (14) (*SI Appendix*, Fig. S11*C*). All these independent loess chronologies yield the same result that the top four loess-paleosol sequences (from L_1 to S_4) correspond to the last four glacial–interglacial cycles. Here, we also obtained the optically stimulated luminescence (OSL) ages of eight samples from the XF section. The results further demonstrate that the loess L_1 layer and paleosol S_1 layer correspond to the last glacial and last interglacial periods, respectively (*SI Appendix*, Table S1 and Fig. S12*A*).

Additionally, a comparison of magnetic susceptibility records between CHJZ and Luochuan (LC) sections, located 160 km apart in the central CLP, has been revealed to closely resemble to each other (58), which is further confirmed by new magnetic susceptibility data and iconic paleosol layers of XF and LC sections (*SI Appendix*, Fig. S12). Detailed OSL dating has been conducted in the LC section spanning the last three loess-paleosol sequences (61, 62) (*SI Appendix*, Fig. S12*B*). These established age models of loess-paleosol sequences in Dongzhiyuan high tableland, along with OSL ages of the XF and LC sections, confirm that the top four loess-paleosol sequences (from L_1 to S_4) correspond to the last four glacial–interglacial cycles. Based on this, we established the primary age model of the XF section by using the rapid shifts in magnetic susceptibility that correspond to the boundaries of MISs recorded by the benthic $\delta^{18}O$ record as tie points for the age model (*SI Appendix*, Figs. S3 and S13). The paleosol S_0, S_1, S_2, S_3, and S_4 layers correspond to the MIS 1, 5, 7, 9, and 11, respectively. Between tie points, the age model was interpolated linearly. For microcodium $\delta^{18}O$ analyses, samples were collected at 5-cm resolution from loess layers (L_2 and L_4) and paleosol layers (S_2 and S_3), corresponding to the interval from ~400 to ~133 ka (*SI Appendix*, Fig. S3).

In addition, microcodium is calcified plant root cells, which likely postdates the surrounding loess and paleosol sequences due to the rooting depth (38). Vegetation on the central CLP is dominated by steppe and most of the root was concentrated at the surface 0–40 cm with a maximum of 20 cm (63). Therefore, here we further refined the chronology of microcodium $\delta^{18}O$ record by subtracting 20 cm in depth, yielding a similar microcodium $\delta^{18}O$ record with that based on the age model of loess-paleosol sequences directly (*SI Appendix*, Fig. S14). Furthermore, the vegetation coverage at glacial–interglacial timescale on the central CLP was always dominated by grasses and shrubs, and the C_4 grasses would slightly increase during the interglacial periods (64), which might slightly change the plant rooting depth and thus the microcodium formation depth. Nevertheless, the microcodium $\delta^{18}O$ record is generally in phase with the summer insolation under glacial and interglacial conditions (Fig. 1), suggesting that the influence of vegetation difference (and thus different microcodium formation depth) on the chronology at orbital timescale may be limited. To assess the influence of microcodium formation depth, we also refined the chronology of microcodium $\delta^{18}O$ record by subtracting 10 and 30 cm in depth, yielding microcodium $\delta^{18}O$ records similar to that refined by subtracting 20 cm (*SI Appendix*, Fig. S14). Therefore, the influence of vegetation difference at glacial–interglacial timescale on the chronology of microcodium $\delta^{18}O$ record is limited. The consistent precession cycles of microcodium and speleothem $\delta^{18}O$ records indicate that the chronology of Chinese loess-paleosol sequences and microcodium $\delta^{18}O$ record at orbital timescale generally is reliable (*SI Appendix*, Fig. S15*A*).

Isotope Analysis. Microcodium was picked at 5-cm resolution for measurements of oxygen isotopes ($\delta^{18}O$) following previous studies (37–39). Oxygen isotopic compositions were analyzed by MAT-253 gas sourced mass spectrometry using a Kiel IV carbonate device at the Nanjing Institute of Geology and Palaeontology, Chinese Academy of Sciences (CAS). $\delta^{18}O$ values were reported relative to the Vienna PeeDee Belemnite (VPDB) standard with a precision of 0.16‰ (2σ).

Composite Microcodium $\delta^{18}O$ Record Over the Last 400 kyr. The new data in this study extended the microcodium $\delta^{18}O$ record (37) from the XF section to the past 400 kyr (*SI Appendix*, Fig. S3*C*). The new data, spanning from ~400 to ~133 ka, vary between −16.83‰ and −9.51‰, which is generally consistent with the previously published record since the last interglacial (from −16.44‰ to −9.29‰) (37). The XF microcodium $\delta^{18}O$ changes agree well with Mangshan microcodium $\delta^{18}O$ during the last glacial and have provided a robust replication test (39) (*SI Appendix*, Fig. S16).

The XF microcodium $\delta^{18}O$ record over the past 400 kyr agrees well with the changes in summer insolation: the $\delta^{18}O$ values are lower during periods of high summer insolation, consistent with speleothem $\delta^{18}O$ records from central southern China (*SI Appendix*, Fig. S15). However, the XF microcodium $\delta^{18}O$ record displays an attenuated precession signal during the interglacial periods. This phenomenon is attributed to the high precipitation and low sediment rate, which lead to intense pedogenesis of the paleosol layers, the associated increase in the dissolution of microcodium, and the attenuation of high-frequency (precession band) signals. On the Loess Plateau, the sediment rate increases, and monsoon precipitation decreases gradually from southeast to northwest along with the monsoon moisture trajectory. The Huanxian (HX) section, located approximately 100 km northwest of the Xifeng section, receives less precipitation, and has a higher sedimentation rate, which reduces the dissolution of microcodium and faithfully captures the precession cycles during interglacial period (38) (*SI Appendix*, Fig. S15).

To better show the precession cycles of precipitation $\delta^{18}O$ during interglacial periods, we replaced the XF microcodium $\delta^{18}O$ record with the previously published HX microcodium $\delta^{18}O$ record (~133–~66 ka) for the last interglacial period (38), yielding a composite microcodium $\delta^{18}O$ record over the last 400 kyr (*SI Appendix*, Fig. S15*B*). At the precession band, the chronology of the composite microcodium $\delta^{18}O$ record was further refined by aligning it with the absolutely dated speleothem $\delta^{18}O$ record within the quoted errors (65) (*SI Appendix*, Fig. S17). As a result, the replacement in the last interglacial leads to a closer match between the composite microcodium and speleothem $\delta^{18}O$ records during the 0 to 200 kyr period compared to the 200 to 400 kyr interval. Both the spectral results of the composite microcodium $\delta^{18}O$ and Xifeng microcodium $\delta^{18}O$ records show the coexistence of 23-, 41-, and 100-kyr periods (*SI Appendix*, Fig. S9 *A* and *C*). In the spectral result of composite microcodium $\delta^{18}O$ record, the 23-kyr signal is more prominent. Nevertheless, here we primarily focus on the distinct low $\delta^{18}O$ values observed during precession minima at peak interglacials, which are evident in both the XF and HX microcodium $\delta^{18}O$ records (*SI Appendix*, Fig. S15). Therefore, this replacement more effectively highlights the precession cycles in microcodium $\delta^{18}O$ record, without altering the distinct low $\delta^{18}O$ values observed during precession minima at peak interglacials.

Spectrum Analysis. We applied the Lomb–Scargle periodograms (66) to calculate power spectra of microcodium and speleothem $\delta^{18}O$ records. The time series used in the analysis were interpolated in step of 1000 y by a Gaussian filter with a SD of the Gaussian window of 0.5 kyr.

Model Simulation. The isotope-enabled Community Earth System Model (iCESM1.3) from the National Center for Atmospheric Research (NCAR) was used to conduct the long-term transient climate simulation for the past 150,000 y. The iCESM is a fully coupled climate model including atmosphere, ocean, land, sea ice, and river runoff components (67). Our model configuration for the experiment is f19_g16. The atmosphere model (CAM5) resolutions are ~1.9° × 2.5° with 30 vertical levels (68). The land model (CLM4) shares the same horizontal grid with the atmosphere model (69). The ocean model (POP2) and sea ice model (CICE4) share the same horizontal grid of a nominal 1° horizontal resolution (70, 71). The ocean model has 60 vertical levels.

Stable water isotopes are incorporated into Community Earth System Model (CESM1.3) through advanced parameterization schemes that represent isotope fractionation mechanisms within the atmosphere (72), ocean (73), land surface (74), river run-off, and sea ice (67). This enables tracking of water isotope ratios, fluxes, and isotopic fractionations across all components of the hydrologic cycle. Consequently, the isotope-enabled model outputs can be directly compared to geological isotope records, bypassing uncertainties inherent in converting isotope

records to other climate proxies (e.g., precipitation). Moreover, the inclusion of water isotopologues provides an independent constraint on simulated atmospheric and hydrologic processes, improving our understanding of the associated processes.

Two experiments with 100-time acceleration were conducted to simulate transient climate change, one with orbital-only forcing and the other with all forcing. In the orbital-only forcing experiment, the model is driven solely by the Earth's orbital parameters. In the all-forcing experiment, the model is forced by Earth's orbital parameters, greenhouse gases, and global ice sheets. For the orbital-only forcing experiment, orbital parameters were initialized at 150 ka and updated at the beginning of each 100-y interval based on the equations of Berger (1978) (75). In the all-forcing experiment, aside from orbital parameters, well-mixed greenhouse gases evolved over time based on reconstructions (17, 76, 77), and continental ice sheets were adjusted according to the ICE-6G reconstruction (78).

The ice sheet evolution since 150 ka used in the model is reconstructed according to the ICE-6G reconstruction since the LGM (78) (*SI Appendix*, Fig. S18). Sea level change curves since 150 ka are compared to those since the LGM based on the LR04 stack benthic $\delta^{18}O$ records (18). For a period when the sea level value since 150 ka closely matched the sea level value since the LGM, the ice sheet distribution during that period is replaced by the corresponding LGM ice sheet reconstruction as widely used (79) (*SI Appendix*, Fig. S18). As the ice sheet volume at the LGM was the largest over the past 150 ka, the range of sea level changes since the LGM generally overlaps with that of the past 150 ka, with a slight excess observed during MIS 5e (*SI Appendix*, Fig. S18). The ice volume evolution since 150 ka was divided into 16 periods, each being replaced by the ice volume corresponding to intervals around 4, 10, 11.5, 14, 15, 17.5, 19.5, and 21 ka, respectively (*SI Appendix*, Fig. S18). This approach provides a reasonable representation of ice sheet evolution on glacial–interglacial timescales. However, uncertainties remain concerning changes in ice sheet area and height. Although the topography and extent of ice sheets influence surface albedo and modulate the meridional temperature gradient, thus affecting the Intertropical Convergence Zone and monsoon precipitation, the extent and mechanisms of their effects may vary slightly (80–82). This may explain the lack of attenuated precession $\delta^{18}O$ minima during the MIS 5a and 5c in comparison to MIS 5e in all-forcing model simulation (*SI Appendix*, Fig. S10).

Given that the response time of the atmosphere–upper ocean system is 1,000 times faster than the shorter orbital cycle, this experiment can mainly capture the long-term monsoon variability (83, 84). The experiment started 170,000 y ago with the first 20,000 y as the spin-up period and the last 150,000 y used for analysis. This model provides seasonally simulated precipitation amount and $\delta^{18}O$ changes, which enables us to assess the seasonal contributions of summer and nonsummer precipitation to the speleothem $\delta^{18}O$ records.

The amount-weighted annual precipitation $\delta^{18}O_a$ is calculated as follows

$$\delta^{18}O_a = \sum_{i=1}^{12} \left(\frac{P_i}{P}\right)\delta^{18}O_i, \quad [1]$$

where i is calendar month, ranging from 1 to 12, P is annual precipitation accumulation, the sum of Pi.

Data, Materials, and Software Availability. The raw paleoclimate data used in this paper is available from East Asian Paleoenvironmental Science Database online (https://doi.org/10.12262/IEECAS.EAPSD2025006) (85).

ACKNOWLEDGMENTS. We thank W.G. Liu, J.J. Zhao, P.X. Shu, and X. Cheng for valuable discussions and X.M. Chen and J. Liu for their help on the oxygen isotope analysis. D.B. Jiang and Michael Rogerson are acknowledged for their valuable suggestions on this work. This research was supported by National Natural Science Foundation of China (NO. 42203062), the Fund of Shandong Province (NO. LSKJ202203300), National Natural Science Foundation of China (NO. 42325302), the Chinese Academy of Sciences (the Youth Innovation Promotion Association of Chinese Academy of Sciences and NO. xbzg-zdsys-202217), the Young Talent Support Plan of Xi'an Jiaotong University, the State Key Laboratory of Loess Science, Chinese Academy of Sciences (NO. SKLLQGPY2404), and U.S. NSF (No. 2303577, 2202860, and 2202913).

Author affiliations: [a]State Key Laboratory of Loess Science, Institute of Earth Environment, Chinese Academy of Sciences, Xi'an 710061, China; [b]Ministry of Education Key Laboratory of Surficial Geochemistry, School of Earth Sciences and Engineering, Nanjing University, Nanjing 210023, China; [c]Department of Geography, Ohio State University, Columbus, OH 43210; [d]School of Geography, Nanjing Normal University, Nanjing 210098, China; [e]Institute of Global Environmental Change, Xi'an Jiaotong University, Xi'an 710049, China; [f]Department of Earth Sciences, University of Minnesota, Minneapolis, MN 55455; [g]Department of Environmental Change, Institute for Innovative Earth Environment Research, Xi'an 710061, China; [h]School of Ecology and Nature Conservation, Beijing Forestry University, Beijing 100083, China; [i]State Key Laboratory of Palaeobiology and Stratigraphy, Nanjing Institute of Geology and Palaeontology, Chinese Academy of Sciences, Nanjing 210008, China; [j]Department of Earth, Environmental, and Planetary Sciences, Brown University, Providence, RI 02912; [k]Interdisciplinary Research Center of Earth Science Frontier, Beijing Normal University, Beijing 100875, China; and [l]National Observation and Research Station of Earth Critical Zone on the Loess Plateau, Xi'an 710061, China

Author contributions: Z.Z., G.L., Y.C., and Z.A. designed research; Z.Z., Z.L., G.L., Q.W., J.L., H.L., Z. Jing, T.L., and S.K. performed research; Z.Z., Z.L., Q.W., and J.L. analyzed data; H.C., R.L.E., S.C.C., Y.W., Y.S., Z.S., L.T., X.W., Z. Jin, and W.Z. provided feedbacks on the analyses, the figures, and the manuscript; and Z.Z., Z.L., G.L., Y.C., Q.W., and Z.A. wrote the paper.

1. H. Cheng *et al.*, The Asian monsoon over the past 640, 000 years and ice age terminations. *Nature* **534**, 640–646 (2016).
2. D. Yuan *et al.*, Timing, duration, and transitions of the last interglacial Asian monsoon. *Science* **304**, 575–578 (2004).
3. Y. Wang *et al.*, The holocene Asian monsoon: Links to solar changes and North Atlantic climate. *Science* **308**, 854–857 (2005).
4. H. Cheng *et al.*, Ice age terminations. *Science* **326**, 248–252 (2009).
5. Y.-J. Wang *et al.*, A high-resolution absolute-dated late Pleistocene monsoon record from Hulu Cave China. *Science* **294**, 2345–2348 (2001).
6. Y. Wang *et al.*, Millennial-and orbital-scale changes in the East Asian monsoon over the past 224, 000 years. *Nature* **451**, 1090–1093 (2008).
7. P. Zhang *et al.*, A test of climate, sun, and culture relationships from an 1810-year Chinese cave record. *Science* **322**, 940–942 (2008).
8. T. Liu, Z. Ding, N. Rutter, Comparison of Milankovitch periods between continental loess and deep sea records over the last 2.5 Ma. *Quat. Sci. Rev.* **18**, 1205–1212 (1999).
9. Z. Ding *et al.*, Ice-volume forcing of East Asian winter monsoon variations in the past 800, 000 years. *Quat. Res.* **44**, 149–159 (1995).
10. J. W. Beck *et al.*, A 550, 000-year record of East Asian monsoon rainfall from ^{10}Be in loess. *Science* **360**, 877–881 (2018).
11. S. C. Clemens *et al.*, Precession-band variance missing from East Asian monsoon runoff. *Nat. Commun.* **9**, 3364 (2018).
12. H. Ao *et al.*, Different orbital rhythms in the Asian summer monsoon records from North and South China during the Pleistocene. *Glob. Planet. Change* **80–81**, 51–60 (2012).
13. Y. Sun *et al.*, Diverse manifestations of the mid-Pleistocene climate transition. *Nat. Commun.* **10**, 352 (2019).
14. W. Zhou *et al.*, Eccentricity-paced geomagnetic field and monsoon rainfall variations over the last 870 kyr. *Proc. Natl. Acad. Sci. U.S.A.* **120**, e2211495120 (2023).
15. Y. Cai *et al.*, Variability of stalagmite-inferred Indian monsoon precipitation over the past 252,000 y. *Proc. Natl. Acad. Sci. U.S.A.* **112**, 2954–2959 (2015).
16. G. Liu *et al.*, On the glacial–interglacial variability of the Asian monsoon in speleothem delta^{18}O records. *Sci. Adv.* **6**, eaay8189 (2020).
17. J.-R. Petit *et al.*, Climate and atmospheric history of the past 420, 000 years from the Vostok ice core Antarctica. *Nature* **399**, 429–436 (1999).
18. L. E. Lisiecki, M. E. Raymo, A pliocene-pleistocene stack of 57 globally distributed benthic $\delta^{18}O$ records. *Paleoceanography* **20**, 1–16 (2005).
19. H. Cheng, A. Sinha, X. Wang, F. W. Cruz, R. L. Edwards, The global paleomonsoon as seen through speleothem records from Asia and the Americas. *Clim. Dyn.* **39**, 1045–1062 (2012).
20. Y. Sun, *et al.*, High-sedimentation-rate loess records: A new window into understanding orbital- and millennial-scale monsoon variability *Earth-Sci. Rev.* **220**, 103731 (2021).
21. J. Laskar *et al.*, A long-term numerical solution for the insolation quantities of the Earth. *Astron. Astrophys.* **428**, 261–285 (2004).
22. E. K. Thomas *et al.*, Temperature and leaf wax δ^2H records demonstrate seasonal and regional controls on Asian monsoon proxies. *Geology* **42**, 1075–1078 (2014).
23. Y. Zheng *et al.*, Decoupled Asian monsoon intensity and precipitation during glacial–interglacial transitions on the Chinese Loess Plateau. *Nat. Commun.* **13**, 5397 (2022).
24. J. C. H. Chiang, M. J. Herman, K. Yoshimura, I. Y. Fung, Enriched East Asian oxygen isotope of precipitation indicates reduced summer seasonality in regional climate and westerlies. *Proc. Natl. Acad. Sci. U.S.A.* **117**, 201922602 (2020).
25. B. A. Maher, Holocene variability of the East Asian summer monsoon from Chinese cave records: A re-assessment. *Holocene* **18**, 861–866 (2008).
26. M. Tan, Circulation effect: Response of precipitation $\delta^{18}O$ to the ENSO cycle in monsoon regions of China. *Clim. Dyn.* **42**, 1067–1077 (2014).
27. Z. Liu *et al.*, Chinese cave records and the East Asia summer monsoon. *Quat. Sci. Rev.* **83**, 115–128 (2014).
28. F. S. R. Pausata, D. S. Battisti, K. H. Nisancioglu, C. M. Bitz, Chinese stalagmite $\delta^{18}O$ controlled by changes in the Indian monsoon during a simulated Heinrich event. *Nat. Geosci.* **4**, 474–480 (2011).
29. S. C. Clemens, W. L. Prell, Y. Sun, Orbital-scale timing and mechanisms driving late Pleistocene Indo-Asian summer monsoons: Reinterpreting cave speleothem $\delta^{18}O$. *Paleoceanography* **25**, PA4207 (2010).
30. W. Duan *et al.*, The transfer of seasonal isotopic variability between precipitation and drip water at eight caves in the monsoon regions of China. *Geochim. Cosmochim. Acta* **183**, 250–266 (2016).
31. A. Baker *et al.*, Global analysis reveals climatic controls on the oxygen isotope composition of cave drip water. *Nat. Commun.* **10**, 2984 (2019).

32. I. J. Orland *et al.*, Direct measurements of deglacial monsoon strength in a Chinese stalagmite. *Geology* **43**, 555–558 (2015).
33. C. He *et al.*, Deglacial variability of South China hydroclimate heavily contributed by autumn rainfall. *Nat. Commun.* **12**, 5875 (2021).
34. T. Caley, D. M. Roche, H. Renssen, Orbital Asian summer monsoon dynamics revealed using an isotope-enabled global climate model. *Nat. Commun.* **5**, 5371 (2014).
35. X. Liu, X. Xie, Z. Guo, Z.-Y. Yin, G. Chen, Model-based distinct characteristics and mechanisms of orbital-scale precipitation $\delta^{18}O$ variations in Asian monsoon and arid regions during late Quaternary. *Natl. Sci. Rev.* **9**, nwac182 (2022).
36. J. C. H. Chiang *et al.*, Role of seasonal transitions and westerly jets in East Asian paleoclimate. *Quat. Sci. Rev.* **108**, 111–129 (2015).
37. Z. Zhang, G. Li, H. Yan, Z. An, Microcodium in Chinese loess as a recorder for the oxygen isotopic composition of monsoonal rainwater. *Quat. Int.* **464**, 364–369 (2018).
38. Z. Zhang, G. Li, Y. Cai, Z. Liu, Z. An, Variation of summer precipitation $\delta^{18}O$ on the Chinese Loess Plateau since the last interglacial. *J. Quat. Sci.* **36**, 1214–1220 (2021).
39. Z. Zhang, *et al.*, Millennial-scale monsoon variability modulated by low-latitude insolation during the last glaciation *Geophys. Res. Lett.* **49**, e2021GL096773 (2022).
40. T. Li, G. Li, Incorporation of trace metals into microcodium as novel proxies for paleo-precipitation. *Earth Planet. Sci. Lett.* **386**, 34–40 (2014).
41. S.-T. Kim, J. R. O'Neil, Equilibrium and nonequilibrium oxygen isotope effects in synthetic carbonates. *Geochim. Cosmochim. Acta* **61**, 3461–3475 (1997).
42. T. L. Poulson, W. B. White, The cave environment. *Science* **165**, 971–981 (1969).
43. F. Peterse *et al.*, Molecular records of continental air temperature and monsoon precipitation variability in East Asia spanning the past 130, 000 years. *Quat. Sci. Rev.* **83**, 76–82 (2014).
44. B. Wu, X. Lang, D. Jiang, Migration of the northern boundary of the East Asian summer monsoon over the last 21, 000 years *J. Geophys. Res. Atmos.* **126**, e2021JD035078 (2021).
45. Y. Cai *et al.*, Orbital- to millennial-scale variation of the speleothem $\delta^{18}O$ record during marine isotope stages 5 to 3 on the southeast Chinese Loess Plateau and its climatic and environmental implications. *J. Quat. Sci.* **38**, 295–307 (2022).
46. Y. Li, *et al.*, Inter-relationship and environmental significance of stalagmite $\delta^{13}C$ and $\delta^{18}O$ records from Zhenzhu Cave, north China, over the last 130 ka *Earth Planet. Sci. Lett.* **536**, 116149 (2020).
47. C. He *et al.*, Hydroclimate footprint of pan-Asian monsoon water isotope during the last deglaciation. *Sci. Adv.* **7**, eabe2611 (2021).
48. H. Zhang, *et al.*, A data-model comparison pinpoints Holocene spatiotemporal pattern of East Asian summer monsoon *Quat. Sci. Rev.* **261**, 106911 (2021).
49. H. Cheng *et al.*, Chinese stalagmite paleoclimate researches: A review and perspective. *Sci. China Earth Sci.* **62**, 1489–1513 (2019).
50. S. C. Priestley *et al.*, Caves demonstrate decrease in rainfall recharge of southwest Australian groundwater is unprecedented for the last 800 years. *Commun. Earth Environ.* **4**, 206 (2023).
51. Y. Ding, Z. Wang, Y. Sun, Inter-decadal variation of the summer precipitation in East China and its association with decreasing Asian summer monsoon. Part I: Observed evidences. *Int. J. Climatol.* **28**, 1139–1162 (2008).
52. H. Zhang *et al.*, East Asian hydroclimate modulated by the position of the westerlies during termination I. *Science* **362**, 580 (2018).
53. T. Li *et al.*, Continued obliquity pacing of East Asian summer precipitation after the mid-Pleistocene transition. *Earth Planet. Sci. Lett.* **457**, 181–190 (2017).
54. W. L. Prell, J. E. Kutzbach, Sensitivity of the Indian monsoon to forcing parameters and implications for its evolution. *Nature* **360**, 647–652 (1992).
55. J. E. Kutzbach, P. J. Guetter, The influence of changing orbital parameters and surface boundary conditions on climate simulations for the past 18 000 years. *J. Atmos. Sci.* **43**, 1726–1759 (1986).
56. Z. An *et al.*, Global monsoon dynamics and climate change. *Annu. Rev. Earth Planet. Sci.* **43**, 29–77 (2015).
57. Y. Sun, S. C. Clemens, Z. An, Z. Yu, Astronomical timescale and palaeoclimatic implication of stacked 3.6-Myr monsoon records from the Chinese Loess Plateau. *Quat. Sci. Rev.* **25**, 33–48 (2006).
58. G. Kukla, Z. An, Loess stratigraphy in central China. *Palaeogeogr. Palaeoclimatol. Palaeoecol.* **72**, 203–225 (1989).
59. Z. An *et al.*, The long-term paleomonsoon variation recorded by the loess-paleosol sequence in central China. *Quat. Int.* **7**, 91–95 (1990).
60. T. Liu, Z. An, B. Yuan, J. Han, The loess-paleosol sequence in China and climatic history. *Int. Union Geol. Sci.* **8**, 21–28 (1985).
61. Y. C. Lu, X. L. Wang, A. G. Wintle, A new OSL chronology for dust accumulation in the last 130,000 yr for the Chinese Loess Plateau. *Quat. Res.* **67**, 152–160 (2007).
62. J. Zhang, Q. Hao, S.-H. Li, An absolutely dated record of climate change over the last three glacial–interglacial cycles from Chinese loess deposits. *Geology* **50**, 1116–1120 (2022).
63. P. Li, Z. Li, M. Hao, L. Zheng, Root distribution characteristics of natural grassland on Loess Plateau. *Research of Soil & Water Conservation* **10**, 144–843 (2003).
64. S. Yang *et al.*, Warming-induced northwestward migration of the East Asian monsoon rain belt from the Last Glacial Maximum to the mid-Holocene. *Proc. Natl. Acad. Sci. U.S.A.* **112**, 201504688 (2015).
65. Z. Zhang *et al.*, A new method for loess chronology by microcodium $\delta^{18}O$ and its application to the Mangshan section. *Quat. Int.* **711**, 32–37 (2024).
66. M. H. Trauth, Spectral analysis in Quaternary sciences *Quat. Sci. Rev.* **270**, 107157 (2021).
67. E. Brady *et al.*, The connected isotopic water cycle in the Community earth system model version 1. *J. Adv. Model. Earth Syst.* **11**, 2547–2566 (2019).
68. R. B. Neale *et al.*, Description of the NCAR community atmosphere model (CAM 5.0). *NCAR Tech.* **1**, 1–12 (2010).
69. K. W. Oleson *et al.*, Technical description of version 4.0 of the community land model (CLM). *NCAR Tech.* **257**, 1–257 (2010).
70. R. Smith *et al.*, The parallel ocean program (POP) reference manual ocean component of the community climate system model (CCSM) and community earth system model (CESM). *LAUR-01853* **141**, 1–140 (2010).
71. E. C. Hunke, Thickness sensitivities in the CICE sea ice model. *Ocean Model.* **34**, 137–149 (2010).
72. J. Nusbaumer, T. E. Wong, C. Bardeen, D. Noone, Evaluating hydrological processes in the Community Atmosphere Model Version 5 (CAM5) using stable isotope ratios of water. *J. Adv. Model. Earth Syst.* **9**, 949–977 (2017).
73. J. Zhang *et al.*, Asynchronous warming and $\delta^{18}O$ evolution of deep Atlantic water masses during the last deglaciation. *Proc. Natl. Acad. Sci. U.S.A.* **114**, 11075–11080 (2017).
74. T. E. Wong, J. Nusbaumer, D. C. Noone, Evaluation of modeled land-atmosphere exchanges with a comprehensive water isotope fractionation scheme in version 4 of the Community Land Model. *J. Adv. Model. Earth Syst.* **9**, 978–1001 (2017).
75. A. Berger, Long-term variations of caloric insolation resulting from the Earth's orbital elements. *Quat. Res.* **9**, 139–167 (1978).
76. L. Dieter *et al.*, High-resolution carbon dioxide concentration record 650, 000–800, 000 years before present. *Nature* **453**, 379–382 (2008).
77. A. Schilt *et al.*, Glacial–interglacial and millennial-scale variations in the atmospheric nitrous oxide concentration during the last 800, 000 years. *Quat. Sci. Rev.* **29**, 182–192 (2010).
78. W. R. Peltier, D. F. Argus, R. Drummond, Space geodesy constrains ice age terminal deglaciation: The global ICE-6G_C (VM5a) model. *J. Geophys. Res. Solid Earth* **120**, 450–487 (2015).
79. E. J. Gowan *et al.*, A new global ice sheet reconstruction for the past 80 000 years. *Nat. Commun.* **12**, 1199 (2021).
80. J. Cao, B. Wang, L. Ma, Attribution of global monsoon response to the last glacial maximum forcings. *J. Climate* **32**, 6589–6605 (2019).
81. J. Cao, B. Wang, J. Liu, Attribution of the last glacial maximum climate formation. *Clim. Dyn.* **53**, 1661–1679 (2019).
82. F. Justino, A. Timmermann, U. Merkel, E. P. Souza, Synoptic reorganization of atmospheric flow during the last glacial maximum. *J. Climate* **18**, 2826–2846 (2005).
83. J. E. Kutzbach, X. Liu, Z. Liu, G. Chen, Simulation of the evolutionary response of global summer monsoons to orbital forcing over the past 280, 000 years. *Clim. Dyn.* **30**, 567–579 (2008).
84. A. Timmermann, S. J. Lorenz, S. I. An, A. Clement, S. P. Xie, The effect of orbital forcing on the mean climate and variability of the tropical Pacific. *J. Climate* **20**, 4147–4159 (2007).
85. Z. Zhang, G. Li, Z. An, Data from "Summer and non-summer climatic signals in speleothem δ18O revealed by loess microcodium δ18O in East Asia". East Asian Paleoenvironmental Science Database. https://doi.org/10.12262/IEECAS.EAPSD2025006. Deposited 26 June 2025.